Received: 25 November 2022 | Revised: 18 July 2023 | Accepted: 4 August 2023

DOI: 10.1002/we.2866

RESEARCH ARTICLE

WILEY

Impact of turbulence and blade surface degradation on the annual energy production of small-scale wind turbines

Ander Zarketa-Astigarraga[1] | Markel Penalba[1,2] | Alain Martin-Mayor[1] | Manex Martinez-Agirre[1]

[1]Faculty of Engineering, Mechanical and Industrial Production, Mondragon Unibertsitatea, Mondragon, Gipuzkoa, Spain

[2]Ikerbasque, Basque Foundation for Science, Bilbao, Spain

Correspondence
Ander Zarketa-Astigarraga, Mondragon Unibertsitatea, Faculty of Engineering, Mechanical and Industrial Production, Loramendi 4, Mondragon, 20500 Gipuzkoa, Spain.
Email: azarketa@mondragon.edu

Funding information
Ekonomiaren Garapen eta Lehiakortasun Saila, Eusko Jaurlaritza, Grant/Award Number: KK-2022/00105; Hezkuntza, Hizkuntza Politika Eta Kultura Saila, Eusko Jaurlaritza, Grant/Award Numbers: IT1505-22, PRE_2017_1_0178

Abstract

Small-scale horizontal axis wind-turbines (SHAWTs) are acquiring relevance within the regulatory policies of the wind sector aiming at net-zero emissions, while reducing visual and environmental impact by means of distributed grids. SHAWTs operate transitionally, at Reynolds numbers that fall between $1 \times 10^5 < Re < 5 \times 10^5$. Furthermore, environmental turbulence and roughness affect the energetic outcome of the turbines. In this study, the combined effect of turbulence and roughness is analysed via wind tunnel experiments upon a transitionally operating NACA0021 airfoil. The combined effects cause a negative synergy, inducing higher drops in lift and efficiency values than when considering the perturbing agents individually. Besides, such losses are Reynolds-dependent, with higher numbers increasing the difference between clean and real configurations, reaching efficiency decrements above 60% in the worst-case scenario.

Thus, these experimental measurements are employed for obtaining the power curves and estimating the annual energy production (AEP) of a 7.8-kW-rated SHAWT design by means of a BEM code. The simulations show a worst-case scenario in which the AEP reduces above 70% when compared to the baseline configuration, with such a loss getting attenuated when a pitch-regulated control is assumed. These results highlight the relevance of performing tests that consider the joint effect of turbulence and roughness.

KEYWORDS
AEP estimation, SHAWT, surface roughness, turbulent effects, wind tunnel experiments

1 | INTRODUCTION

1.1 | Context and motivation

The growth in the interest of renewable energies as substitutes for fossil fuels gets particularly reflected on the global trends of the wind energy industry. The year 2022 witnessed a 77.6 GW of installed capacity worldwide, almost reaching the symbolic milestone of 1 TW in operation.[1] Such a threshold is already far from the 825 MW of globally installed wind power that reports of 2022 were highlighting,[2] which indicates a rapid

increase in the deployment of wind-turbines. Usually, such power capacities follow from a technological strategy based on building larger turbines, giving rise to the large-scale wind turbine (LSWT) industry. In fact, modern wind turbine versions are much larger, with rotor blade diameters up to eight times larger than those of the 1980s as a primary means of increasing the power output.[3]

Yet, the LSWT sector does not provide the full picture of the wind industry. The small-scale wind turbine (SSWT) branch has been acquiring an increasing relevance within the wind-energy sector lately.[4] According to the worldwide-accepted stipulation by the American Wind Energy Association (AWEA), SSWTs are those turbines with a rated power of up to 100 kW, which, translated into dimensions, corresponds to a maximum rotor diameter of 20 m.[5] Compared to the multi-MW output and over 100-m-long diameters of current LSWTs, the capacities of SSWTs may seem negligible, but their recent global increase and widespread use deserves special attention. Especially in the United States and the European countries, policies stimulating the inclusion of electric power from SSWTs have been encouraged by governmental institutions, mainly on the scope of pushing self-sufficient and decentralized power generation systems within the green deal strategy of the European Union.[6–8] The appeal of a self-sufficient prospection is linked to the rise of environmental concerns, such as the global warming due to the increase of greenhouse gas emissions or the visual impact they induce. On the scope of the net-zero-emission agreements by 2050 within the LSWT sector,[9] technological investments in favour of the small-scale industry are justified as a complimentary way of achieving such goals, primarily within urban and isolated environments, where deploying SSWT-based distributed grids should have a reduced environmental impact.[8] It is on these grounds that the 950 MW of global installed capacity achieves relevance, with the SSWT sector having undergone a growth-rate far over 50% during 2013–2018.[4,7]

1.2 | Scale-effect issues

In contrast to LSWTs, which are usually installed in large farms far from the consumers, SSWTs are often installed isolated or in small arrays, mainly in urban areas that constitute the so-called electrical grid islands. Consequently, the operating conditions vary significantly with respect to LSWTs, with two main aspects being worth of mention. The first has to do with the scaling of the devices: when it comes to the aerodynamic behaviour of the blades, the smaller dimensions of the components make them operate at much lower Reynolds numbers than their LSWT counterparts.[10,11] Recent studies show that typical Reynolds numbers based on small-scale horizontal-axis wind turbine (SHAWT) blade chords lie below 500k,[11] with values falling as low as 47k.[12] Databases comprising a wide number of airfoils operating at such Reynolds numbers have been largely used,[13,14] with updated versions of lift, drag and pressure coefficient curves being widely employed nowadays.[15,16] Under such Reynolds conditions, the flow is known to lie within the so-called *transitional regime*, with complex structures being formed upon its surface.[16–18] The transitional regime stands between the laminar and turbulent regimes and shows an interplay between the fluid structures formed upon both of them. The usual picture of an airfoil subjected to a transitional flow consists of a short laminar extent near the leading-edge of the airfoil, followed by a separated shear-layer that reattaches to the surface in the form of a turbulent boundary-layer downstream, producing what is known as a laminar separation bubble in between.[19,20] Such a bubble is known to be highly sensitive to flow conditions, its position depending strongly on the Reynolds number, the geometry of the airfoil and the freestream conditions.[18,20,21] This sensitivity of the bubble gets reflected on the aerodynamic behaviour of the airfoil, whose lift and drag coefficients show a noticeable dependence on the Reynolds number, even at Reynolds variations as low as 20k.[18] Despite such a pronounced scale-effect, SHAWT designers have not been dissuaded from building ever-more efficient turbines, with the hope of overcoming the limitations imposed by transitional flows. A recent review lists over 70 studies dealing with the design issues aimed at improving SHAWT behaviour,[11] and further research published since shows that the interest on the sector prevails.[12,22–24]

1.3 | Flow-perturbing agents: turbulence and roughness

The other aspect that compromises the aerodynamic behaviour of wind turbines is the operation site. In LSWTs, the effect of environmental agents compromises both the aerodynamic behaviour of the turbine blades, due to the incoming flow variations induced by turbulent eddies or the geometrical modifications caused by phenomena such as icing,[25–29] and the subsequent control of the turbine system as a whole, leading to the need of developing holistic control techniques that take into account the effect of the perturbing agents.[30,31]

Regarding SHAWTs, urban environments are known to be highly turbulent,[32–39] with turbulence intensities being capable of reaching values as high as 15%[32,33] depending on the terrain and orography of the environment.[36–38] The situation is not dissimilar in LSWTs, which may face relatively smaller turbulent intensities but, nonetheless, the non-Gaussian or intermittent features of the eddies get manifested on both the decrease of the output power and the fatigue loads of the blades.[40,41] Nevertheless, such a clear consensus does not seem to hold when considering the effect of turbulence on SHAWTs. For some authors, there is a threshold on the turbulent intensity below which the power output decreases, and vice versa.[34] Others report a descent of the power curves regardless of the turbulent conditions,[35] and develop models that predict the optimum installation sites upon buildings with the aim of minimizing losses.[36] Finally, there are studies showing an increase in the power output due to turbulent effects, which may lie between 10% and 122% depending on the specific operation conditions.[38] However, this increase in the outcome is

accompanied by higher fatigue loads (between 32% and 105%) and lower lifetime expectancies of the blades,[38] a downside that is expected to have played the same role in the rest of the case-studies. Those fatigue loads are said to come from the intermittent features of the freestream turbulence being transferred to the rotor torque and bending moments, which require a careful consideration accordingly.[39] The dissent on the results about the energetic outcomes seems to stem from the inability of the underlying IEC 61400-2 standard model for describing the turbulent field properly.[34,37,38,42] Such a model is put into question by some researchers,[37,38] and further experimental tests on SHAWTs subjected to turbulent conditions are deemed necessary for completing the description.[38,39]

In addition to turbulent effects, urban environments with high airborne particle densities are known to affect wind turbines causing debris accumulation or surface erosion, phenomena that are grouped under the broader notion of surface roughness, downgrading the aerodynamic behaviour of the blades.[43–47] For instance, the effect of insect debris accumulation is shown to halve the power outcome of wind turbines.[43] The same goes for sand particles accumulated upon the blades operating in dusty places, such as desert-like environments, causing up to 50% power reduction within a lapse of 9 months after installation.[44] The affected region is shown to be focused on the leading-edge of the airfoil, covering a larger extent in the chordwise dimension with increasing operation times.[44] Instead of accumulation, agents such as rain, hail or airborne particles can induce surface erosion, which impacts differently on the energetic outcome. On the grounds of LSWT devices, debris accumulation is shown to occur in blade sections subjected to relatively slow wind velocities, producing a lift decrease of 34% and a drag penalty of 159% in the worst-case scenario.[45] The same study shows that erosion, which is present on the near-tip sections owning larger relative velocities, causes a 53% lift decrease and a 314% drag increase instead. In terms of annual energy production (AEP), such a blade degradation is shown to cause a 2% loss when subjected to erosion, increasing to 3.7% when debris accumulation is present. Although the mentioned case corresponds to a LSWT device, accumulation and erosion patterns are acknowledged to have similar effects on SHAWTs,[46,47] with the power coefficient decreasing up to 23.7% and considering the additional handicap that the degraded blades are liable to produce acoustic emissions.[46] As occurs with turbulence-related effects, surface roughness issues can be addressed either empirically, through experimental tests[46,48–50] and field-related data,[51–53] or via numerical simulations.[45,54,55] Nonetheless, roughness-accounting simulations are computationally demanding, and they usually require empirically-derived data for reproducing the spatial and temporal distributions of roughness-inducing environmental agents.[45,54]

The variable aerodynamic behaviour within the transitional region, coupled with the effects caused by turbulence and roughness, causes highly demanding fatigue loads and surface damages. The affected blades are required to undergo inspections and repairs, which are accounted as operation and maintenance (O&M) costs of the system.[56,57] In the case of LSWTs, operations such as blade cleaning or surface coating can reach rates as high as $30k per blade,[58] with the devices requiring overhauls each 2-5 years and giving rise to a global O&M market expected to grow as large as $27 billion by 2025.[57] Nevertheless, the SSWT sector acknowledges that operation and maintenance costs are different; operation costs correspond, among lease payments and insurance taxes alike, to the remote monitoring of the system, whereas maintenance costs refer to repairs and their related issues.[56] The main difference between them is that operation expenses are not substantial for SSWT distributed projects, but maintenance costs can reach values of up to $43/kW/year for SHAWTs.[56] Thus, it is expectable that, instead of the corrective actions redounding to maintenance costs, wind engineers will prefer to adopt preventive O&M strategies that could leverage the expenses by focusing them on the monitoring and control of wind turbines. Designing such strategies requires addressing the effects that flow regime variations, turbulence and roughness induce on the aerodynamic behaviour of the blades, as well as the impact that such alterations have on the energetic outcome of the turbines. Within a state-of-the-art that lacks an integral methodology for estimating these effects without field data, developing a systematic experimental approach on roughness-accounting tests becomes as crucial as in the turbulence-related studies.

In addition to this procedural gap in the current state-of-the-art, to the best of the authors' knowledge, little attention has been paid to dealing with the combined effects of turbulence and roughness on transitionally-operating airfoils that correspond to SHAWT blades, apart from the studies undertaken in previous works.[22,23] Such studies, together with those mentioned above, address either of the effects individually, but do not consider their joint contribution to the downgrading of the aerodynamic behaviour and the prospection of AEP losses. Nevertheless, the fact that both turbulence and roughness effects are relevant is not questioned according to the provided evidence. However, the available bibliography assumes the mutual independence of both factors, as if turbulence and roughness effects do not interact with each other. The main purpose of the present study is to show that such is not the case, asserting the synergistic relation arising from the combined introduction of turbulence and roughness effects. In addition, a hybrid experimental-numerical approach is developed for accurately estimating the impact of these combined effects on the performance of SHAWTs and their AEP loss.

For such a purpose, the framework of the research is set in a twofold approach. On the one side, wind tunnel experiments are carried out upon a NACA0021 profile, representative of SHAWT blades, subjected to different transitional Reynolds numbers and flow paradigms that go from clean conditions to real configurations considering turbulence and roughness. Airfoil polars, namely the lift (c_l) and drag (c_d) coefficients, are obtained for a range of typical SHAWT operation conditions subjected to the different flow paradigms. On the other side, those polars are extrapolated for estimating the AEP losses of common SHAWT designs by means of the blade-element-momentum-based (BEM) open-source code QBlade,[59] which is widely employed by SHAWT designers.[60,61] For easy reference and conceptualization, this twofold experimental-numerical framework is schematically represented in Figure 1.

Thus, the rest of the paper is structured as follows: Section 2 presents the general framework of the research, dealing with both the experimental set-up, measurement protocols and the methods used for reproducing the different flow paradigms, as well as with the numerically

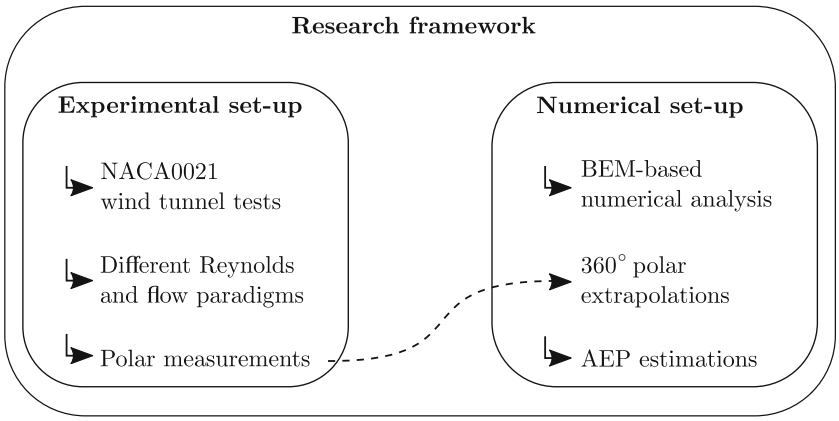

FIGURE 1 Schematic framework of the research.

configured blades for the AEP loss estimations. Section 3 outlines the SHAWT employed as a case-study for the AEP loss estimations. Section 4 deals with the results and their corresponding discussions, and, finally, Section 5 synthesizes the main findings of the work and suggests possible future research lines.

2 | RESEARCH FRAMEWORK

As mentioned in Section 1, the general research framework comprises two main approaches that are detailed herein: Section 2.1 copes with the experimental set-up, wind tunnel subtleties and measurement issues, whereas Section 2.2 is devoted to presenting the numerical approach.

2.1 | Experimental set-up

The experiments are performed in an open-circuit wind tunnel facility with a rectangular cross-section of 0.75×1 m^2 and a 3-m-long test-section. A 37-kW fan drives the system, producing flows with peak velocities of 40 m/s and turbulence levels below 0.2%. For illustrative purposes, Figure 2 represents a schematic draft of the set-up. Further particularities of the wind tunnel are available in previous studies.[62,63]

The model employed in the experiments consists of a three-part modular assembly owning a chordwise dimension of $c = 150$ mm and a span of $s = 900$ mm. The NACA0021 geometry of the airfoil has been chosen because of its standard use in wind turbine-related aerodynamic studies.[10,17,64,65] The flow conditions at the leading-edge of the airfoil are established by computing its chord-based Reynolds number. The user-settable fan power determines the incoming flow's velocity, which is measured by a *Delta-Ohm HD49047T01L* Pitot-static probe. Temperature, pressure and relative humidity, recorded at the inlet of the test-section with a *Delta-Ohm HD2001.1* ambient conditions transmitter, allow computing the density and viscosity of the air.

The airfoil is placed vertically on the test-section and fixed to a *Kistler 9119AA2* piezoelectric balance that measures the loads acting upon the model. The balance is mounted atop a rotary plate and controlled by a *NI ISM 7400* stepper motor, achieving control over the angle-of-attack of the airfoil (α). The endplates delimiting the model ensure the two-dimensionality of the flow.[66] Due to the large lift-to-drag ratios featured by the airfoils[67,68] and the inherent cross-coupling of the piezoelectric balance,[69] a *Scanivalve MPS4264* type differential pressure scanner owning 64 ports and placed atop the wind tunnel is employed for drag measurements. A holder placed downstream the endplates houses an *Aerolab* 18-port wake-rake. The holder is attached to a 3D-positioning system driven by three *NI ISM 7400* stepper motors, allowing to traverse the rake across the tunnel's width and to measure the drag coefficient by surveying its wake via the momentum-deficit method.[70] The thickness of the endplates is such that the blockage-ratio of the airfoil at the maximum tested angle-of-attack, namely 20°, lies below 10%, with wall-interference corrections being applied according to the scheme proposed by Selig et al.[15] The synchronization and monitoring of the distinct devices is achieved by *National Instruments* data-acquisition and control modules, with a LabVIEW[71] application employed for setting the required flow configurations and scheduling the measurements.

The configuration illustrated in Figure 2 corresponds to a steady, two-dimensional and uniform airstream. Such a clean flow paradigm constitutes a baseline case-study, but does not represent the real flow conditions that wind turbines face on their operation sites. The experimental reproduction of those conditions requires, as explained in Section 1, implementing two perturbing agents upon the clean flow configuration: turbulence and roughness. Turbulent effects are included by means of a passive grid installed at the inlet of the test-section, providing intensity (I)

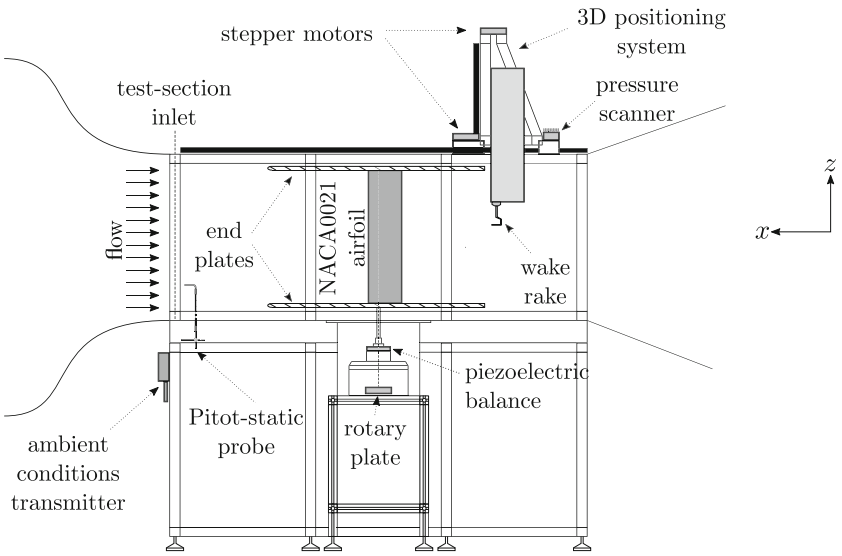

FIGURE 2 Schematic illustration of the wind tunnel set-up for undertaking measurements upon an airfoil.

TABLE 1 Parametrical schedule for the experimental testing campaign.

Flow paradigm	Reynolds number	Angular config.	Turbulence intensity	Roughness chordwise coverage
Clean	$\mathrm{Re} \in [0.8,1,1.2] \cdot 10^5$	$\alpha \in [0,20]^\circ$	Default (0.2%)	–
Turbulent			$I = 3.8\%$	–
Rough		$\Delta\alpha = 1^\circ$	Default (0.2%)	10%
Real			$I = 3.8\%$	10%

levels at the leading-edge that reach values of $\approx 4\%$[68] that are representative of low intensity conditions.[32,33] Surface-roughness is considered by attaching a P80 type sandgrain paper band with an average grain height of ≈ 100 μm to the airfoil, disposing it symmetrically around the 10% chordwise extent of the leading-edge in accordance to the coverage values provided in Khalfallah and Koliub.[44] Although roughness effects are known to be non-symmetric,[44,45] keeping the airfoil symmetrical allows for a direct contrasting with datasets obtained from configurations without roughness effects, enabling a valid qualitative comparison framework. The implementation of turbulence and roughness effects leads to four different flow paradigms owning increasing levels of complexity and closeness to realistic conditions:

- Clean flow paradigm (referenced as *Clean* whenever it addresses experimental or numerical data pertaining this configuration): considers neither turbulent nor roughness effects. It constitutes the ideal baseline of comparison for the rest of the paradigms.
- Turbulent flow paradigm (named *Turbulent* hereon): includes turbulent effects solely and is representative of scenarios on which the turbine blades have not been degraded by roughness effects so far, such as the initial period of operation after the deployment of wind turbines.
- Rough flow paradigm (named *Rough*): considers roughness effects merely. It constitutes an intermediate, pseudo-real configuration that may prove useful for highlighting roughness-exclusive effects.
- Real flow paradigm (named *Real*): it combines the turbulent and roughness effects and aims at addressing the conditions encountered in wind turbine blades that have been active for an extended operation period.

The experimental tests undertaken for each of the flow paradigms consider three different Reynolds numbers, namely, $\mathrm{Re} = [0.8,1,1.2] \times 10^5$, which correspond to the restricted interval imposed by the passive grid.[68] The possible turbulent configurations are limited to a unique value of $I = 3.8\%$, corresponding to the maximum turbulence intensity achievable at the leading-edge. The real configuration is obtained by combining the $I = 3.8\%$ turbulent intensity case with the 10% coverage roughness band. The angular variations of c_l and c_d are obtained for each of those case-studies, yielding the $c_l - \alpha$ and $c_d - \alpha$ characteristic curves. The angular route defined for the tests covers the $\alpha \in [0,20]^\circ$ range, performing steps of $\Delta\alpha = 1^\circ$. Table 1 summarizes the multi-parametrical field that determines the experimental testing campaign.

The repeatability of the experiments is ensured by undertaking three different tests for each configuration. The quantitative results presented in Section 4 correspond to the average values obtained from those three datasets. Complying with the uncertainty-related principles laid in

previous works,[63,72] the datasets have been statistically analysed for obtaining the uncertainty intervals that correspond to a 95% confidence level. The maximum and mean values of the flow-paradigm-dependent c_l- and c_d-related uncertainty intervals, as well as their standard deviations, are provided in Table 2.

2.2 | Numerical set-up

2.2.1 | BEM-based workflow

The estimation of AEP losses is carried out numerically by means of implementing the BEM theory,[73,74] with the resultant workflow being shown in Figure 3. The open-source QBlade code[59] has been used for such a purpose, its main parts comprising a three-step procedure in which the dataflow evolves from left to right:

- The purpose of the leftmost processing block is twofold: First of all, the user defines the airfoil objects that will comprise the blades of the wind turbine to be analysed. The geometrical specifications of the airfoils, such as their camber or thickness, are established in this step. Once the airfoils are initialized, their respective polars, or $c_l - c_d$ curves, must be either computed or supplied by the user. In the present study, $c_l - c_d$ relations coming from wind-tunnel experiments are employed.
- The polars obtained in the first processing block are then extrapolated for covering the 360° angular extent. In customary experimental tests, it is usual to employ angles-of-attack that do not increase beyond 15–20, as such a range corresponds to the angular extent at which wind turbine blades perform under design operation conditions. As turbine-related calculations and, particularly, AEP estimations require knowing the behaviour of the blades for the full angular range, the commonly used Viterna extrapolation approach[75] is employed for extending the polars.
- Once the 360° polars are obtained, the user configures a blade design by stipulating the desired airfoil geometries and their coverage across the span, which constitutes the baseline for constructing the rotor object. The aerodynamic behaviour of the blades is then simulated by following the BEM theory, and the rotor performance is obtained by simulating the device over a range of incoming wind speeds. The AEP estimation is performed by stipulating a given Weibull distribution[76] for the statistical modelization of the rates at which different wind speeds occur, which is a distribution that has been amply adopted by the wind community for such a purpose.[77]

TABLE 2 Maximum, mean and standard deviations of the uncertainty intervals.

	c_l-related			c_d-related		
Flow paradigm	$\delta_{c_{l_{max.}}}$	$\overline{\delta_{c_l}}$	$\sigma_{\delta_{c_l}}$	$\delta_{c_{d_{max.}}}$	$\overline{\delta_{c_d}}$	$\sigma_{\delta_{c_d}}$
Clean	0.1676	0.1523	7.14×10^{-3}	5.27×10^{-2}	2.42×10^{-2}	1.55×10^{-2}
Turbulent	0.1642	0.1626	2.45×10^{-3}	0.1216	3.81×10^{-2}	3.2×10^{-2}
Rough	0.1633	0.1616	7.14×10^{-3}	4.38×10^{-2}	2.1×10^{-2}	1.44×10^{-2}
Real	0.1595	0.1569	3.11×10^{-3}	0.1371	5.09×10^{-2}	3.13×10^{-2}

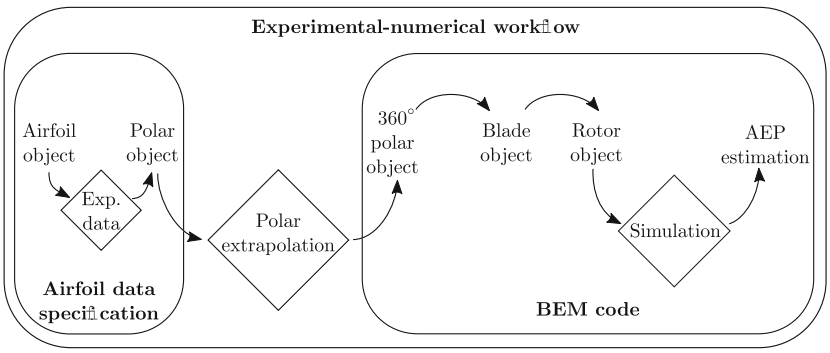

FIGURE 3 Schematic of the experimental-numerical workflow philosophy followed by QBlade.[59]

3 | CASE-STUDY

3.1 | Turbine selection

The sequential workflow described in Section 2.2.1 stresses the relevance of the geometry of the airfoils and the shape of the turbine blades for undertaking AEP calculations. The case-study analysed herein considers a three-bladed SHAWT inspired by the study of Habali and Saleh,[78] who outline a detailed procedure for designing a SHAWT blade. They specify a linearly decreasing spanwise variation of the chord, and a nearly parabolic trend for the blade's twist. The twist values proposed in the mentioned study have been maintained, setting a root-tip variation that goes from 16° to an untwisted configuration, respectively. The chord dimension has been scaled so that the spanwise variation of the Reynolds number falls within the experimentally tested range, yielding a root-tip distribution that starts at 160 mm and ends with a 54-mm chord. A 800-mm root-wise extent is provided for coupling the rotor to the hub, resulting in an effective blade span of 4.2 m. The employed blades comprise a 5-m-radius rotor and, for the chord distribution employed in the present research, the resultant wind turbine owns a rated wind speed of 11 m/s and a rotational velocity of 75 rpm, which yield a design tip-speed ratio (λ) of 3.8 and a rated power of 7.8 kW. The cut-in speed is set to 2.5 m/s, and the maximum velocity limit at 15 m/s. Figure 4A shows both the edgewise and flapwise views of the blade, with the chord and twist values specified at 10%-equispaced stages along the effective span dimension. Figure 4B represents, under nominal conditions, the spanwise-varying chord-based Reynolds number at each blade section. The turbine is considered to operate, nominally, under a stall-regulated control, resulting in an average AEP of 30 MWh when facing clean-flow conditions. The nominal control mechanism, that is, stall regulation, is based on the fact that blade sections lose performance at increasing wind speeds due to a decrease of their lift values and an increase of the drag, which is an aerodynamic effect known as stall and propagates from the hub outwards. In addition to stall-regulated control, the turbine is also simulated under a pitch-regulated mechanism, which corresponds to an active control system that varies the pitch angle of the turbine blades at high wind speeds, achieving to maintain a constant output power beyond a predefined wind speed value.

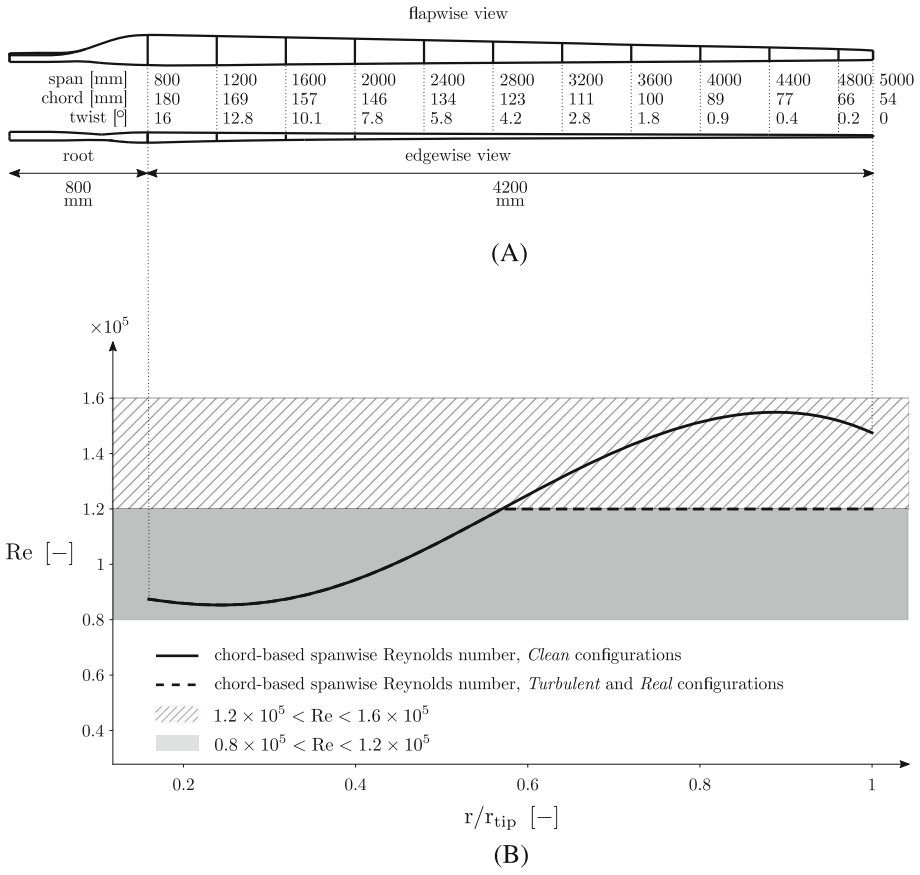

FIGURE 4 Blade-related parameters; (A) chosen blade design; (B) spanwise-varying chord-based Reynolds number.

3.2 | Simulation parameters

Given the scale-effect observed in transitionally operating airfoils[18] and the noticeaeble Reynolds variation that, according to Figure 4B, ensues along the span, the blade is discretized into $N = 100$ equispaced elements for considering the Reynolds dependency of the polars. The polars of the blade elements subjected to Reynolds numbers that fall between the testing values are obtained by interpolation, which cover the entire range in the *Clean* cases. As for the *Turbulent* and *Real* cases, their effect can only be considered within the inwards half of the span, due to the technical limitations of the wind-tunnel facility that constrain the Reynolds number to values below 1.2×10^5 when the turbulence-generating-grid is present. A previous work by the authors has shown that the aerodynamic features of the NACA0021 airfoil tested herein evolve non-linearly within the transitional region,[18] being unable to determine their variations via extrapolation with acceptable precision. Accordingly, the polars of the outer half of the blade sections, when they are operating under either *Turbulent* or *Real* conditions, are considered to be those that correspond to the respective data sets obtained at $\mathrm{Re} = 1.2 \times 10^5$, as represented by the straight dashed line that parts from the mid spanwise dimension in Figure 4B.

The power curves and AEP performances are analysed for 11 different case-studies: two of them address the blade under clean and turbulent conditions. The stall-regulated clean configuration is regarded as the baseline or nominal case, whereas the turbulent configuration is interpreted as the one under which the turbine operates *in situ* while not having been affected by roughness yet. The rest of the cases constitute a set of 9 configurations showing a progressively larger blade area operating under *Real* (turbulence + roughness) conditions, beginning from a 10% of the tipwards section and progressive inwards until covering the whole span. Each configuration is simulated under stall- and pitch-regulated controls. In the case of the latter, the pitch control is imposed beyond the maximum power.

The shape (k) and scale (A) parameters of the Weibull distribution are set to $k = 2$ and $A = 8.13$ m/s, which match the orders of magnitude of the distributions employed in SHAWT applications[35] and provide the nominal AEP of 30 MWh for the clean blade configuration. Table 3 summarizes the geometrical- and simulation-related parameters of the computed case-studies.

4 | RESULTS AND DISCUSSION

This section consists of two parts: Section 4.1 analyses the aerodynamics of the NACA0021 airfoil under different flow paradigms, focusing on the main behaviour variations shown by the model. Section 4.2 applies such an analysis to the SHAWT described in Section 3, predicting the impact of varying the flow paradigm on the AEP losses by means of a BEM-based approach.

4.1 | Aerodynamic behaviour analysis

The flow-paradigm-dependent characteristic curves, following an increasing order of the tested Reynolds numbers, are provided in Figures 5–7. The layout of the figures intends to ease the comparison between the plotted parameters on a single sight. Figures 5A, 6A, and 7A show the $c_l - \alpha$ curves obtained at each Reynolds number. Figures 5B, 6B, and 7B correspond to the $E - \alpha$ curves, with $E = c_l/c_d$ standing for the aerodynamic efficiency of the airfoil, which is a surrogate for the output/input energies to the system. The employed representations for the $c_l - \alpha$ and $E - \alpha$ curves correspond to the one that the QBlade code uses when initializing an airfoil and have been kept for the sake of consistency. There are certain aspects of the curves that are relevant for determining the performance of the wind turbine and the estimation of the AEP. Proceeding sequentially:

- **Lift curves:** The Reynolds-dependent evolution observed in Figures 5A, 6A, and 7A shows that turbulent and roughness effects play different roles, which have been remarked in Figure 5A. Taking the *Clean* paradigm as the baseline case, turbulence is shown to delay stall considerably, and to induce larger c_l values at low Reynolds numbers. This fact gets attenuated at higher Reynolds configurations, up to the point of causing a slight loss in the maximum lift value, namely, $c_{l_{\max}}$, at $\mathrm{Re} = 1.2 \times 10^5$. Instead, roughness effects seem to cause a progressively larger drop on the lift values, as well as promoting stall noticeably when increasing the Reynolds number. The *Real* curves show that the combination of both effects is additive when it comes to the $c_l - \alpha$ relations; indeed, both the stall delay and the c_l drop are observed in the curves, resulting in a superposed effect of both perturbing agents. One last aspect worth of being mentioned is the straightening of the linear region of the curves, which happens for every flow-paradigm other than the *Clean* one and yields c_l values that are much lower than the baseline case at low angles-of-attack. Being the lift force the aerodynamic mechanism whereby a wind turbine produces its energetic output, the mentioned differences on the $c_l - \alpha$ curves allow foreseeing the behaviour that the system will have under distinct flow paradigms. Indeed, both perturbing agents induce a poor behaviour at low angles-of-attack, with the baseline case showing the ability to produce a considerably larger amount of energy. However, the altered stalling characteristics of the *Turbulent* and *Real* cases show the potential to maintain larger lifts at high angles-of-attack, a fact that may partially compensate for their low performance at small α values, which can grow as large as 37% at between the *Clean* and *Real* cases at Re1.2×10^5.

TABLE 3 Numerical parameters for the QBlade-simulated rotor.

	Rotor-related parameters
Rotor design	Habali & Saleh[78] inspired
Rotor blades	3
Blade length	5000 mm
Blade geometry	NACA0021
Blade chord	Linear root-tip variation:
	from 160 to 54 mm
Blade twist	Nearly parabolic root-tip variation:
	from 16° to untwisted
Cut-in speed	2.5 m/s
Cut-off speed	15 m/s
Nominal speed	11 m/s
Nominal rotational speed	75 rpm
Nominal λ	3.8
Nominal power	7.8 kW
Nominal AEP	30 MWh
Regulation	Stall-regulated
	Pitch-regulated
	Simulation-related parameters
# blade elements	100
Polar spec.	Experimental
Weibull parameters	$k = 2$
	$A = 8.13$ m/s
Case-studies	
Flow-paradigm	**Affected coverage (from tip to root)**
Clean	0%
Turbulent	0%
Real	$\in [10,100]\%, \Delta = 10\%$

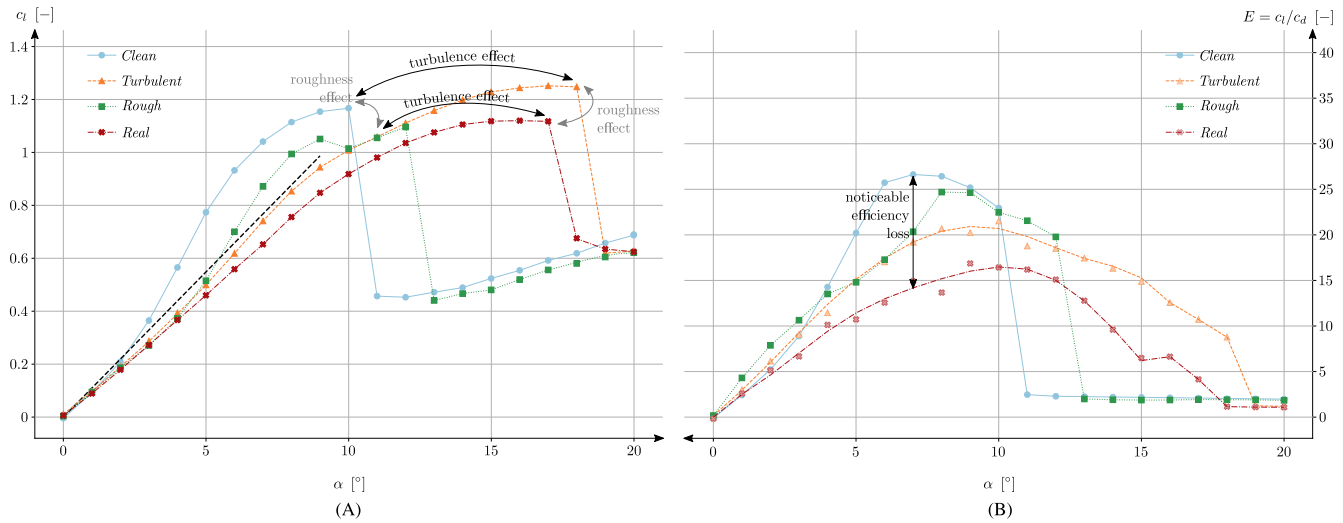

FIGURE 5 Flow-paradigm-dependent $c_l - \alpha$ (A) and $E - \alpha$ (B) curves at Re=0.8×10^5.

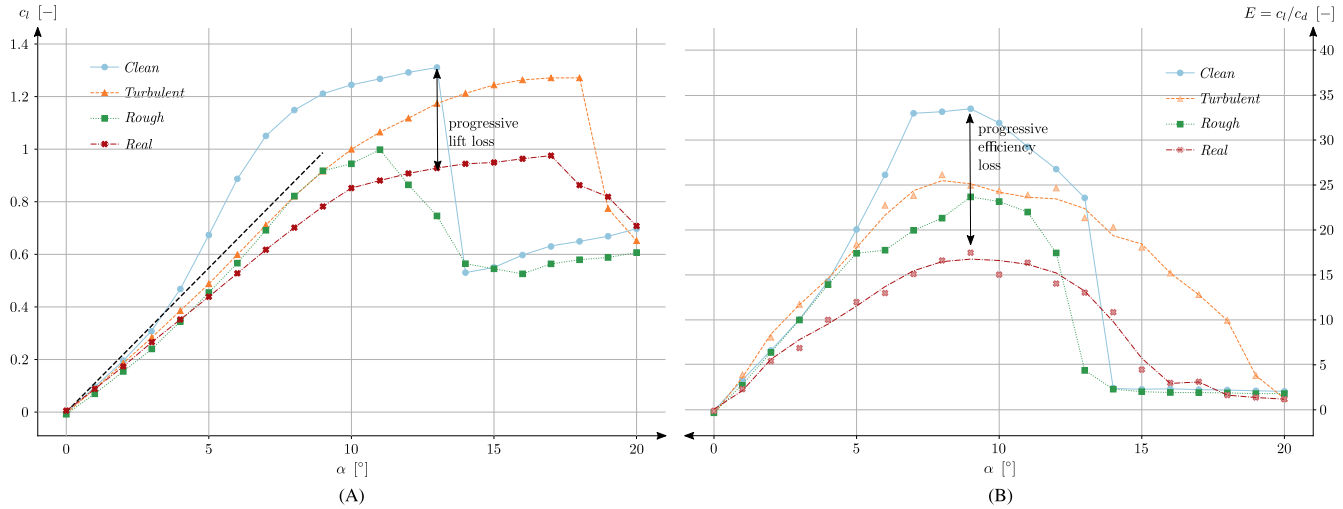

FIGURE 6 Flow-paradigm-dependent $c_l - \alpha$ (A) and $E - \alpha$ (B) curves at Re=1×10^5

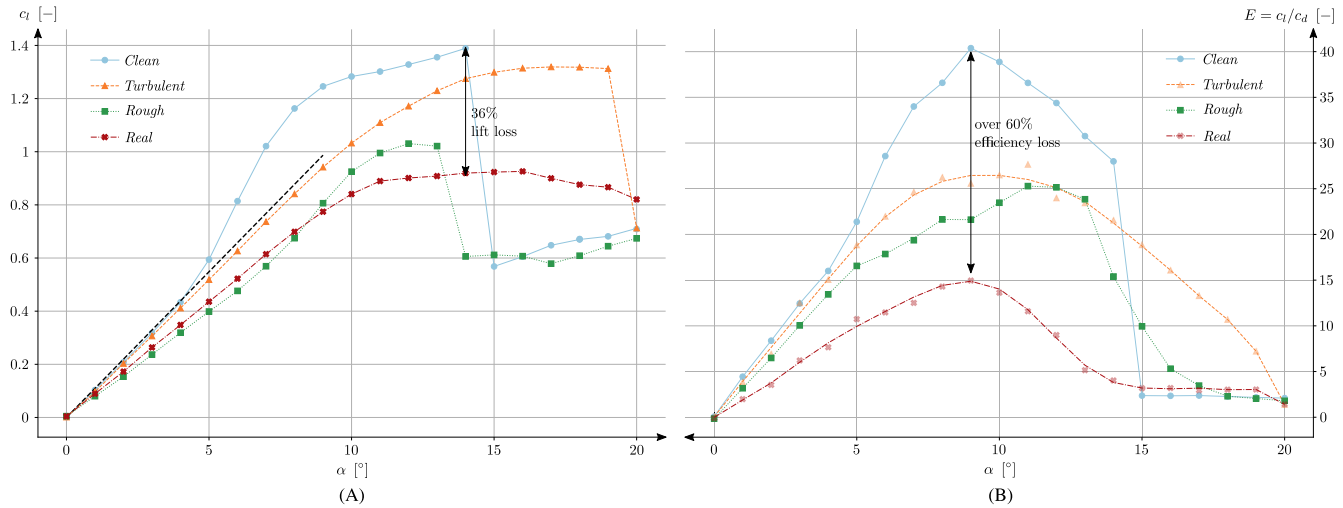

FIGURE 7 Flow-paradigm-dependent $c_l - \alpha$ (A) and $E - \alpha$ (B) curves at Re $= 1.2 \times 10^5$.

- **Efficiency curves:** The Reynolds-dependent evolution shown in Figures 5B, 6B, and 7B manifests certain differences with respect to the $c_l - \alpha$ plots. The most relevant is that the effects of turbulence and roughness are not as clearly discernible as in the lift cases. The stall delay, observed in the *Turbulent* and *Real* cases of the $c_l - \alpha$ curves, remains almost unaltered in the efficiency ones, except for the *Real* paradigm at Re $= 1.2 \times 10^5$ that shows a largely degraded behaviour throughout the tested angular range. But the c_l drop caused by roughness effects is not reproduced equally in the $E - \alpha$ curves, with the efficiency values of the *Turbulent* and *Rough* cases matching considerably within the low- and mid-α range. The result of this is that the *Real* paradigm does not show an additive interplay of both perturbing agents but rather a synergistic one. The efficiency drop due to the combined effect of turbulence and roughness can be larger than the sum of their individual contributions, especially at large Reynolds numbers. Furthermore, the maximum efficiency drop surpasses the 60% at Re $= 1.2 \times 10^5$, whereas it does not reach the 40% decrease in c_l values. If the aerodynamic efficiency is interpreted as the capacity to extract the available energy from the incoming flow, the degraded efficiencies of the $E - \alpha$ curves can be understood as a poorer ability to convert the overall work performed by the lift force into a net power output.

Figure 8 is a synthesis of the most relevant aerodynamic parameters that have been analysed above, namely: the maximum lift coefficient ($c_{l_{max.}}$), efficiency ($E_{max.}$) and the stalling angle-of-attack (α_{stall}), which are shown in Figure 8A–C, respectively. The *x*-axis represents the Reynolds number, and the data pertaining to each flow paradigm correspond with the depicted bars.

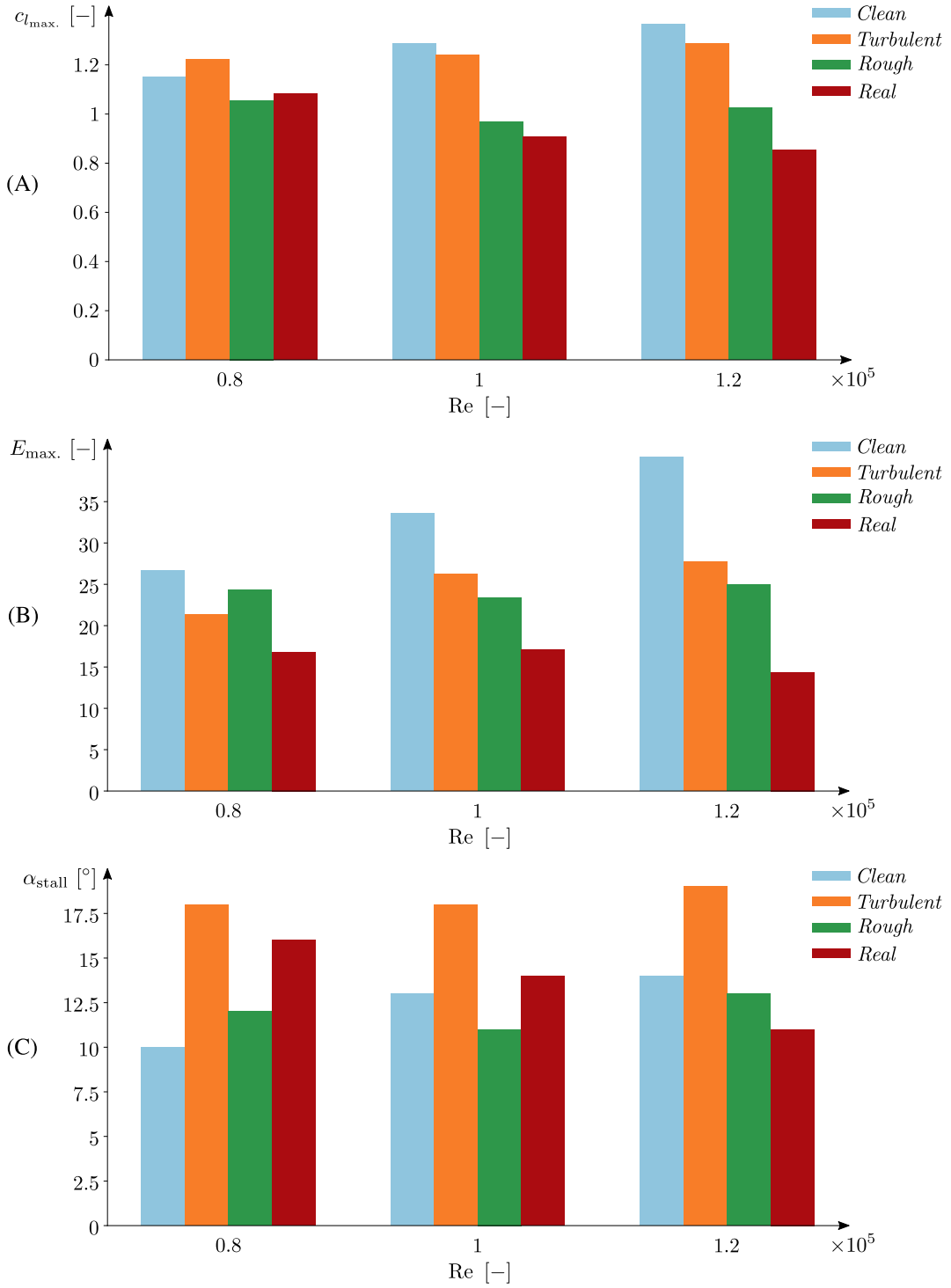

FIGURE 8 Synthesis of Reynolds- and configuration-dependent aerodynamic parameters: (A) maximum lift coefficient, $c_{l_{max.}}$; (B) maximum efficiency, $E_{max.}$; (C) stall angle, α_{stall}.

- $c_{l_{max.}}$ evolution: The sustained increase observed in the *Clean* configurations, which shows a sensible scale-effect, gets attenuated when turbulence is present, and becomes erratic when considering roughness effects. Although no physical mechanism is devised for explaining such a behaviour, it seems to underlie the synergistic effect that comes into play when combining turbulence and roughness, given that the *Real* paradigm is the only configuration that shows a sustained decrease with the Reynolds number. Furthermore, for $Re \geq 1 \times 10^5$, the paradigms show a progressively decreasing trend when displayed in the *Clean-Turbulent-Rough-Real* order. This ordering indicates that roughness effects are more effective on perturbing the flow and deviating it from the baseline case, and that roughness may be playing a more relevant role on the

synergistic phenomenon than turbulent sources. It is evident that the c_l-related power extraction capabilities of wind turbine blades subjected to transitional Reynolds numbers are severely affected by both the scale-effect and the flow paradigm.

- $\mathbf{E_{max.}}$ evolution: The efficiency trends reproduce the behaviours observed in the $c_{l_{max.}}$ evolutions, although in a somewhat different manner. The scale-effect is noticeably more pronounced for the *Clean* paradigm, whereas the *Turbulent* configurations show a slow increase in comparison. The same occurs with the erratic trends of the *Rough* configurations, with differences among them being relatively concealed and tending towards a seemingly constant evolution. These stagnant evolutions of the *Turbulent* and *Rough* paradigms stem from the larger values of their drag coefficients, which counteract the effect of potential lift increments and hinder the ability of the efficiency parameter to grow as in the *Clean* paradigm. The synergistic effect is as observable as in the $c_{l_{max.}}$ parameter, although the stagnant evolutions mentioned for the *Turbulent* and *Rough* cases are also reproduced by the *Real* configurations. If the $c_{l_{max.}}$ trends indicate a progressive lowering on the power outcome of transitionally-operating blades, the $E_{max.}$ parameter shows that such a decrease is accompanied by a higher ratio of the input/output energies of the system, leading to a higher cost per kW produced.
- $\boldsymbol{\alpha_{stall}}$ evolution: it is representative of the strong synergistic effect undergone by the *Real* configurations. Indeed, α_{stall} experiences a sustained increase in the case of the *Clean* paradigm, in accordance to the acute scale-effect explained in[18] that leads to an enlarged pre-stall regime. The *Turbulent* paradigm is effective in delaying stall, showing a wider pre-stall region that barely changes with the Reynolds number. However, the *Rough* configurations keep yielding a non-monotonous evolution, with a decreasing trend at low Reynolds numbers that turns into an increasing one afterwards. As occurs for the lift and efficiency evolutions, it seems that such a trend accounts for the sustained decrease observed in the *Real* cases, although the manner in which turbulent and rough effects interplay requires a further explanation. With all, it is to be determined whether the increased pre-stall region of the *Turbulent* and *Real* configurations is beneficial for the wind turbine system.

The analysis above shows that the consideration of different flow paradigms affects greatly the aerodynamic behaviour of the airfoil, which suggests that the energetic outcome of the wind turbine will be equally compromised by the environmental agents. Furthermore, the synergistic effect observed between turbulence and roughness turns mandatory to design and test the blades under flow conditions that lie as close as possible to realistic configurations, were their aerodynamic behaviour not to be largely overpredicted.

4.2 | Power curves and AEP loss estimations

The results of the simulations carried out by means of the QBlade code are synthesized in two charts: the power curves shown in Figure 9 and the AEP estimations depicted in Figure 10. The discussion below considers them sequentially:

- **Power curves:** the curves shown in Figure 9 represent the power output of the different wind turbine configurations when subjected to a range of incoming air speeds. The solid lines correspond to the wind turbine being stall-regulated, which is why those curves fall continuously

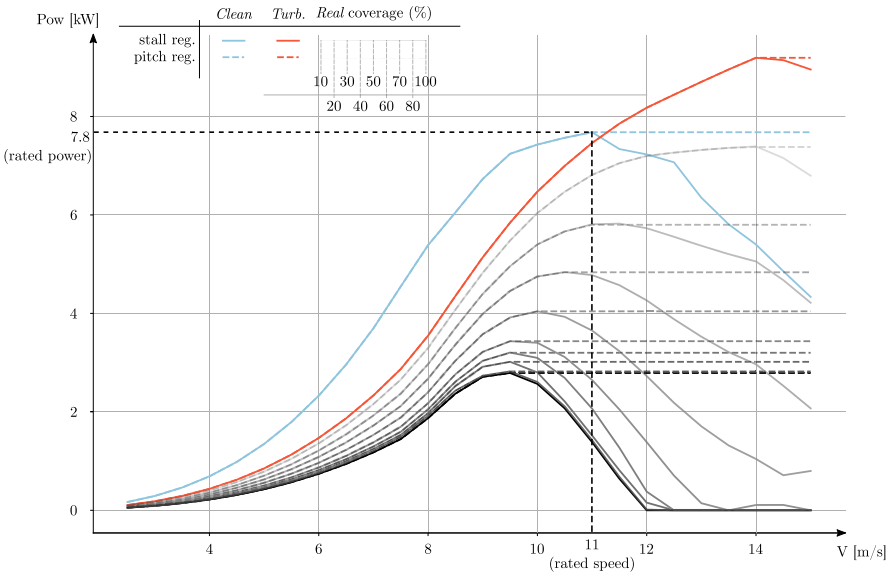

FIGURE 9 Power curves for the simulated configurations.

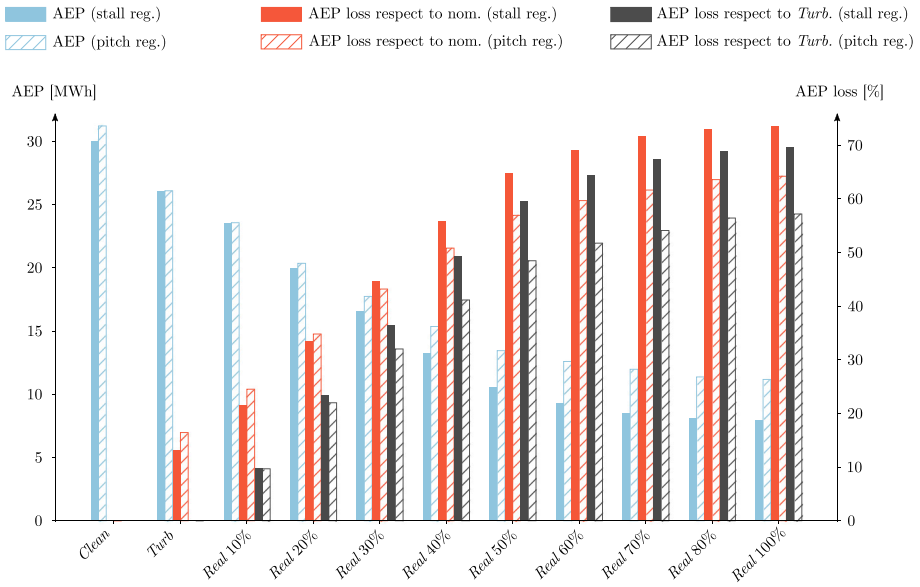

FIGURE 10 Estimated AEPs and AEP losses for the simulated configurations.

once surpassing the inflow velocity at which the maximum power is obtained. The dashed lines address the pitch-regulated simulations, with the pitch mechanism entering each wind turbine configuration at its maximum power point. Thus, both curve families become discernible beyond such a point, with the pitch-regulated cases achieving to maintain the maximum power value until the cut-off air speed.

As observed, the baseline configuration provides the rated 7.8 kW at the nominal velocity of 11 m/s. However, the *Turbulent* configuration is capable of increasing the maximum power to 9 kW, obtained at a larger wind speed of 14 m/s. This is mainly due to the stall delay induced by turbulent effects, as shown in Figures 5–7. Nevertheless, such a gain in maximum power is rapidly lost when roughness effects come into play, with the case of the 10% coverage *Real* configuration already showing a power peak below the rated value, although the velocity at which such a peak occurs lies above the rated wind speed. Anyhow, the velocity corresponding to the peak power falls below the rated speed for *Real* cases with coverages beyond 30%, decaying progressively in a manner similar to the power maxima. This is certainly due to the smaller c_l values that occur at moderate inflow speeds, which make the blades operate at low angles-of-attack and, consequently, within the linear region of the $c_l - \alpha$ curve. The analysis on Section 4.1 has shown the noticeably poorer behaviour of the *Real* configurations within such a range. Despite the *Real* configurations showing a delayed stall similar to the *Turbulent* cases, the overall lowering of the power curves may be straightforwardly related to the noticeably poorer behaviour of the *Real* configurations observed in the $E - \alpha$ curves.

On this respect, it is to notice that the mentioned lowering of the power curves saturates progressively. The departure from the *Turbulent* curves is more pronounced for the *Real* cases owning up to 50% coverage. Thence, larger spanwise extents operating under real conditions do not affect the overall curves as sensitively. This is a clear indicative of the tipwards blade sections being the largest contributors to the power output of the wind turbine.

The features mentioned so far lead to an interpretation of the control mechanisms. The differences between the stall- and pitch-regulated curves become significant in *Real* configurations with coverages above 50%. Indeed, the lowering of the wind speed at which the maximum power value is achieved makes the pitch-regulated control more effective when the turbine is severely damaged. In contrast, it is to observe the little effect that such a control mechanism has upon the *Turbulent* configuration, not succeeding to obtain an appreciable gain over the stall-regulated mechanism.

- **AEP estimations:** Figure 10 shows the synthesis of the AEP estimations for the simulated configurations, with the *x*-axis indicating the considered case-study and the left-side *y*-axis indicating the AEP value in MWh. Additionally, the right-side *y*-axis stands for the AEP loss in a per-unit basis, taking either the clean configuration or the turbulent one as a baseline. Losses with respect to the clean configuration are interpreted as those occurring due to differences between the turbulent or real configurations and the nominal ones. Instead, losses with respect to the turbulent configuration correspond to discrepancies in the *in situ* operation conditions, given that a newly installed wind turbine would be facing a turbulent flow along its entire span, without showing any roughness-related damage. The solid bars refer to the stall-regulated cases, whereas the hatched ones address the pitch-regulated ones.

  It is to notice, first of all, that the AEP values estimated for the *Turbulent* configurations are lower than their *Clean* counterparts, even though the power curves described in Figure 9 show a higher maximum power for the *Turbulent* cases. However, the AEP estimation results from the

convolution of the power curves with the Weibull function, which represents the wind speed frequency distribution. When carrying out such a convolution, the lower power values of the *Turbulent* configuration outweigh the effect of the increase in maximum power, resulting in a decreased AEP estimation overall. The discrepancy between an increased maximum power value and a lower AEP estimation may have relevant consequences at the design stage. Had the design process not have been carried out by considering *Clean* conditions alone, but by devising the behaviour that the blade would have under the *in situ* turbulent conditions, the spanwise distribution of the chords, twists and airfoil geometries may had been chosen so that the blade could show an improved behaviour when operating at *Turbulent* configurations. Thus, this combined interpretation of the power curves and AEP estimations shows the relevance of undertaking the design process with a consistent choice of the flow paradigm that the blade will encounter in its operation site.

Besides such an aspect, the other features highlighted in the power curves get corroborated in the AEP estimations. In particular, the exponential decay of the AEP becomes manifest, with the largest decrease taking place within the 10%–50% coverage of the *Real* cases and saturating afterwards. Those are the configurations which correspond to the tipwards blade sections becoming affected by roughness effects, with the turbine losing its most relevant contributors to the power output. The nominal AEP value of 30 MWh drops approximately to 7.5 MWh when employing a stall-regulated turbine, causing a loss above 70% in what constitutes the worst case scenario.

The pitch-regulated cases follow a similar trend, albeit producing an AEP that lies slightly above the stall-regulated configurations for the *Clean* and *Turbulent* cases, as well as for the lowest coverage values of the *Real* cases. As mentioned before, the pitch-based control becomes relevant when the blades are severely damaged. On this respect, it is worth mentioning that the loss attenuation achieved by switching the control mechanism can lie above 10% in the most critical scenario. Indeed, the 7.5 MWh estimated for the overly damaged case under a stall-regulated mechanism rise beyond 10 MWh when employing a pitch-based control. This lowers the >70% loss mentioned before to 60%, which, although still appreciable, constitutes a non-negligible gain with respect to the stall-regulated case.

The above analysis shows that the influence of the flow conditions upon the aerodynamic polars are propagated to the AEP estimations of wind turbines through their effects on the power curves. However, such a propagation need not be straightforward. The interaction between different blade sections, and the subsequent integration of their respective aerodynamic behaviours into such global parameters as power curves or AEP values, introduce additional effects on the analysis that turn the correspondence between those global parameters and $c_l - \alpha$ or $E - \alpha$ merely qualitative. On this respect, the outlined methodology calls for performing a thorough study of the wind turbine system, beginning from its airfoil-level aerodynamics and scaling it up until reaching the energetic scope of the turbine.

Additionally, the analysis highlights the convenience of employing a control mechanism other than the stall-regulated one, especially when the blades are largely damaged. However, it also opens a research line when it comes to considering mechanisms other than the pitch-regulated one. As shown, the pitch-based regulation is effective when considering damage coverages beyond 50%. However, the largest AEP decays occur earlier, during the lifetime of the turbine within which the blades majorly lose their power-generating capacity due to the damage of the tipwards sections. On this respect, it would be convenient to devise control mechanism that would prevent such a loss, be it by a scheduling blade overhauls and repairs adequately, be it by designing active flow-control techniques by which the aerodynamic curves would not be as severely affected because of turbulent and roughness effects as in the cases analysed in this research.

5 | CONCLUSIONS AND FUTURE WORKS

The research undertaken herein has shown a twofold purpose: The first one has addressed an experimental analysis upon the aerodynamic behaviour of a transitionally operating airfoil under a set of different flow-paradigms and Reynolds numbers. The main findings of such an analysis are listed below:

- The scale-effect becomes evident beyond $\mathrm{Re} = 1 \times 10^5$, with the lift and efficiency coefficients of the flow-paradigm-dependent curves adopting an increasingly degraded nature according to the *Clean-Turbulent-Rough-Real* order.
- The synergistic interplay between turbulence and roughness turns manifest in the overly degraded behaviour of the *Real* curves. In the worst case scenario, which corresponds to $\mathrm{Re} = 1.2 \times 10^5$, the maximum efficiency difference between the *Clean* and *Real* configurations grows larger than 60%.
- The decay on the maximum lift and efficiency values when going from *Clean* to *Real* curves is progressive, whereas the stalling angle does not show such a marked trend. This shows that mechanisms affecting stall may not be as straightforward to assess as the synergistic effect observed in the c_l and E trends.
- The need for performing wind tunnel tests under a set of flow conditions as realistic as possible turns mandatory if blade airfoils are not to be designed with an overpredicted behaviour.

The second purpose of the work has been to carry out a set of numerical simulations on a SHAWT by means of the QBlade code, in order to estimate the AEP losses due to changes on the flow conditions to which the blades are subjected. The numerical analysis has yielded the following findings:

- A thorough methodology, covering from airfoil-level aerodynamics to a turbine-level analysis, is mandatory for studying the behaviour of a wind turbine under realistic flow conditions.
- Employing airfoil-level data obtained under flow conditions as realistic as possible is a prerequisite for a design process aimed at determining a turbine's blade shape that will deploy its full potential when installed in situ.
- The major contributors to the power output of the turbine are the blade sections situated beyond the 50% of the span dimension. When roughness effects are introduced progressively inwards from the tip, it is the damage of the outer half of the blade which induces the largest decrease on both the power curve and the estimated AEP values.
- The worst case corresponds to the overall damaged blade operating under the stall-regulated mechanism. Both the rated power and the AEP decrease above 70%, and the maximum power drops slightly above 65%.
- Power and AEP losses saturate when considering damages on the inwards sections of the blade, which are not as relevant as the outer ones.
- The pitch-regulated mechanism is capable of mitigating the losses considerably, especially when the damage occurs at the inward sections of the blade. The worst case scenario is shown to attenuate its AEP drop from 72% to 60% when changing the control mechanism.
- Despite the relative efficacy of the pitch-regulated mechanism for attenuating the losses, it turns necessary to devise alternative control techniques capable of acting upon the aerodynamic curves, thus preventing the large losses that occur when the outer halves of the blades get damaged.

Having accounted for the main goals of the study, it is due time to remark the limitations encountered when carrying out the experimental campaign, as well as the potential future lines identified both for overcoming such limitations and for complementing the current study with additional tests.

- Both the implementation of the turbulent effects and the testing Reynolds range are limited by the physical and mechanical constraints of the experimental facility. A turbulent intensity of $\approx 4\%$ may not be representative enough of realistic conditions encountered in small-scale wind-turbine locations, and developing stronger eddies turns necessary for bringing the experimental campaign closer to in situ configurations. Likewise, the tested Reynolds interval is limited to $0.8 \times 10^5 < \mathrm{Re} < 1.2 \times 10^5$, mainly due to the power constraints of the tunnel. Adapting the experimental facility for allowing the extension of turbulent intensity levels and Reynolds intervals would suppose an important step forward.
- In accordance to the above limitation, the polars employed in the current study have made used of experimental measurements within a limited range of angles-of-attack, namely $-20^\circ \leq \alpha \leq 20^\circ$. Such a reduced range is usually employed due to the interest of the linear $c_l - \alpha$ relationship that ensues within. However, it demands either analytical or semiempirical approaches for extrapolating the polars to 360°, which is a mandatory requirement if the rotor behaviour and the AEP are to be estimated. A potential enhancement of the current experimental procedure is to devise testing campaigns with angles-of-attack spanning the overall range, thus getting rid of the uncertainties introduced by the usage of extrapolation approaches.
- If the two points mentioned so far consider facility-related limitations, the roughness band implemented as a way of emulating surface degradation constitutes a design choice of the testing campaign. So does the usage of the NACA0021 geometry as the airfoil's cross-section. Both choices, the leading-edge-centered roughness coverage of 10% and the NACA0021 geometry, have been duly justified when presenting the experimental set-up in Section 2.1. However, they limit the validity of the results to such configurations and, consequently, the conclusions drawn in the study must be applied to other airfoils and surface degradation levels with care.
- Finally, the large efficiency losses measured and the corresponding AEP drops call for implementing some sort of flow-control technique for trying to mitigate such detrimental effects. An actual research line undertaken by the group considers the implementation of discrete roughness elements. Such elements, akin to the so-called vortex generators, specifically engineered for preventing stall and enhancing the aerodynamic behaviour of the airfoil when operating under the most critical conditions.

ACKNOWLEDGEMENTS

The authors gratefully acknowledge the financial support from the Department of Education of the Basque Government for the Research Grant [PRE_2017_1_0178] and the Research Group [No. IT1505-22], as well as the support of the Economic Development, Sustainability and Environment Department of the Basque Government under the the Grant [KK-2022/00105].

PEER REVIEW

The peer review history for this article is available at https://www.webofscience.com/api/gateway/wos/peer-review/10.1002/we.2866.

ORCID

Ander Zarketa-Astigarraga https://orcid.org/0000-0002-8183-6154

Markel Penalba https://orcid.org/0000-0002-8396-7334

REFERENCES

1. Zhao F, Hutchinson M. GLOBAL WIND REPORT 2023, Global Wind Energy Council (GWEC); 2023.
2. Renewable Capacity Statistics 2022, International Renewable Energy Agency (IRENA); 2022.
3. Amirzadeh B, Louhghalam A, Raessi M, Tootkaboni M. A computational framework for the analysis of rain-induced erosion in wind turbine blades, part I: stochastic rain texture model and drop impact simulations. *J Wind Eng Ind Aerodyn*. 2017;163(September 2016):33-43.
4. Bianchini A, Bangga G, Baring-Gould I, et al. Current status and grand challenges for small wind turbine technology. *Wind Energy Sci Discuss*. 2022; 2022:1-54.
5. AWEA Small Wind Turbine Global Market Study, American Wind Energy Association (AWEA); 2010.
6. Ruggiero S, Varho V, Rikkonen P. Transition to distributed energy generation in Finland: prospects and barriers. *Energy Policy*. 2015;86:433-443.
7. Moreira Chagas CC, Giannini Pereira M, Pinguelli Rosa L, Fidelis da Silva N, Vasconcelos Freitas MA, Hunt JD. From megawatts to kilowatts: a review of small wind turbine applications, lessons from the US to Brazil. *Sustainability*. 2020;12(2760):1-25.
8. Torres-Madroñero JL, Alvarez-Montoya J, Restrepo-Montoya D, Tamayo-Avendaño JM, Nieto-Londoño C, Sierra-Pérez J. Technological and operational aspects that limit small wind turbines performance. *Energies*. 2020;13(22):1-39.
9. Lee J, Zhao F. GLOBAL WIND REPORT 2021, Global Wind Energy Council; 2021.
10. Tummala A, Kishore R, Kumar D, Indraja V. A review on small scale wind turbines: a review on small scale wind turbines. *Renew Sustain Energy Rev*. 2020;56(July):1351-1371.
11. Arumugam P, Ramalingam V, Bhaganagar K. A pathway towards sustainable development of small capacity horizontal axis wind turbines—identification of influencing design parameters & their role on performance analysis. *Sustain Energy Technol Assess*. 2021;44(January):101019.
12. Hamlaoui MN, Smaili A, Dobrev I, Pereira M, Fellouah H, Khelladi S. Numerical and experimental investigations of HAWT near wake predictions using Particle Image Velocimetry and Actuator Disk Method. *Energy*. 2022;238:121660.
13. Selig MS, Donovan JF, Fraser DB. *Airfoils at Low Speeds*. Virginia Beach, VI, U.S.A: H.A. Stokely; 1989.
14. Selig MS. New airfoils for small horizontal axis wind turbines. *ASME J Solar Energy Eng*. 1998;120:1-7.
15. Selig M, Deters R, Wiliamson G. Wind tunnel testing airfoils at low Reynolds numbers. In: 49th AIAA Aerospace Sciences Meeting; 2011; Orlando, FL, U.S.A.
16. Ananda G, Sukumar P, Selig M. Measured aerodynamic characteristics of wings at low Reynolds numbers. *Aerosp Sci Technol*. 2015;42:392-406.
17. Du L, Berson A, Dominy RG. Aerofoil behaviour at high angles of attack and at Reynolds numbers appropriate for small wind turbines. *Proc Inst Mech Eng, Part C: J Mech Eng Sci*. 2015;229(11):2007-2022.
18. Zarketa-astigarraga A, Penalba M, Martin-mayor A, Martinez-agirre M. Experimental assessment of scale-effects on the aerodynamic characterization of a transitionally-operating airfoil working under clean flow conditions. *Measurement*. 2022;188(December 2021):110414.
19. Gaster M. The Structure and Behaviour of Laminar Separation Bubbles, London, UK, Aeronautical Research Committee (ARc); 1967.
20. Horton HP. Laminar separation bubbles in two and three dimensional incompressible flow. *Ph.D. Thesis*: Queen Mary University of London; 1968.
21. Winslow J, Otsuka H, Govindarajan B, Chopra I. Basic understanding of airfoil characteristics at low Reynolds numbers (104–105). *J Aircr*. 2018;55(3): 1050-1061.
22. Guo T, Guo X, Gao Z, Li S, Zheng X, Gao X, Li R, Wang T, Li Y, Li D. Nacelle and tower effect on a stand-along wind turbine energy output: a discussion on field measurements of a small wind turbine. *Appl Energy*. 2021;303(August):117590.
23. Jiang Y, Liu S, Zao P, Yu Y, Zou L, Liu L, Li J. Experimental evaluation of a tree-shaped quad-rotor wind turbine on power output controllability and survival shutdown capability. *Appl Energy*. 2022;309(December 2021):118350.
24. Zaki A, Abdelrahman MA, Ayad SS, Abdellatif OE. Effects of leading edge slat on the aerodynamic performance of low Reynolds number horizontal axis wind turbine. *Energy*. 2022;239:122338.
25. Gillenwater D, Masson C, Perron J. Wind turbine performance during icing events. In: 46th AIAA Aerospace Sciences Meeting and Exhibit; 2008:1-9.
26. Rindeskär E. Modelling of icing for wind farms in cold climate. *Tech. Rep*. 201; 2010.
27. Yirtici O, Tuncer IH. Aerodynamic shape optimization of wind turbine blades for minimizing power production losses due to icing. *Cold Reg Sci Technol*. 2021;185:103250.
28. Stoyanov DB, Nixon JD, Sarlak H. Analysis of derating and anti-icing strategies for wind turbines in cold climates. *Appl Energy*. 2021;288(January): 116610.
29. Swenson L, Gao L, Hong J, Shen L. An efficacious model for predicting icing-induced energy loss for wind turbines. *Appl Energy*. 2022;305(April 2021): 117809.
30. Peri E, Tal A. A sustainable way forward for wind power: assessing turbines' environmental impacts using a holistic GIS analysis. *Appl Energy*. 2020; 279(September):115829.
31. Keighobadi J, Mohammadian H, Naseradinmousavi P. Adaptive neural dynamic surface control for uniform energy exploitation of floating wind turbine. *Appl Energy*. 2022;316(2021):119132.
32. Watkins S, Ravi S, Loxton B. The effect of turbulence on the aerodynamics of low Reynolds number wings. *Eng Lett*. 2010;18(3):279.
33. Watkins S, Thompson M, Loxton B, Abdulrahim M. On low altitude flight through the atmospheric boundary layer. *Int J Micro Air Veh*. 2010;2(2): 55-68.
34. Lubitz WD. Impact of ambient turbulence on performance of a small wind turbine. *Renew Energy*. 2012;61:69-73.
35. Pagnini LC, Burlando M, Repetto MP. Experimental power curve of small-size wind turbines in turbulent urban environment. *Appl Energy*. 2015;154: 112-121.
36. Yang AS, Su YM, Wen CY, Juan YH, Wang WS, Cheng CH. Estimation of wind power generation in dense urban area. *Appl Energy*. 2016;171:213-230.
37. Anup KC, Whale J, Urmee T. Urban wind conditions and small wind turbines in the built environment: a review. *Renew Energy*. 2019;131:268-283.

38. Anup KC, Whale J, Evans SP, Clausen PD. An investigation of the impact of wind speed and turbulence on small wind turbine operation and fatigue loads. *Renew Energy*. 2020;146:87-98.
39. Anup KC, Whale J, Peinke J. An investigation of the impact of turbulence intermittency on the rotor loads of a small wind turbine. *Renew Energy*. 2021;169:582-597.
40. Schottler J, Reinke N, Hölling A, Whale J, Peinke J, Hölling M. On the impact of non-Gaussian wind statistics on wind turbines—an experimental approach. *Wind Energy Sci Discuss*. 2016;2007:1-21.
41. Schwarz CM, Ehrich S, Peinke J. Wind turbine load dynamics in the context of turbulence intermittency. *Wind Energy Sci*. 2019;4(4):581-594.
42. Castellani F, Astolfi D, Becchetti M, Berno F, Cianetti F, Cetrini A. Experimental and Numerical Vibrational Analysis of a Horizontal-Axis Micro-Wind Turbine; 2018.
43. Corten GP, Veldkamp HF. Aerodynamics: Insects can halve wind-turbine power. *Nature*. 2001;412(6842):41-42.
44. Khalfallah MG, Koliub AM. Effect of dust on the performance of wind turbines. *Desalination*. 2007;209:209-220.
45. Han W, Kim J, Kim B. Effects of contamination and erosion at the leading edge of blade tip airfoils on the annual energy production of wind turbines. *Renew Energy*. 2018;115:817-823.
46. Latoufis K, Riziotis V, Voutsinas S, Hatziargyriou N. Effects of leading edge erosion on the power performance and acoustic noise emissions of locally manufactured small wind turbine blades. *J Phys: Confer Ser*. 2019;1222(1):1-12.
47. Curci R, Bruno P, Carmo S. Analysis of wind turbine blade aerodynamic optimization strategies considering surface degradation. *J Braz Soc Mech Sci Eng*. 2021;43(10):1-22.
48. Bartolomé L, Teuwen J. Prospective challenges in the experimentation of the rain erosion on the leading edge of wind turbine blades. *Wind Energy*. 2019;22(1):140-151.
49. Mohamed Elhadi I, Mamoun M. Water droplet erosion of wind turbine blades: mechanics, testing, modeling and future perspectives. *Materials*. 2020; 13(157):1-33.
50. Law H, Koutsos V. Leading edge erosion of wind turbines: effect of solid airborne particles and rain on operational wind farms. *Wind Energy*. 2020; 23(10):1955-1965.
51. Hasager C, Vejen F, Bech JI, Skrzypiński WR, Tilg AM, Nielsen M. Assessment of the rain and wind climate with focus on wind turbine blade leading edge erosion rate and expected lifetime in Danish Seas. *Renew Energy*. 2020;149:91-102.
52. Shankar Verma A, Jiang Z, Ren Z, Caboni M, Verhoef H, van der Mijle-Meijer H, Castro SGP, Teuwen JJE. A probabilistic long-term framework for site-specific erosion analysis of wind turbine blades: a case study of 31 Dutch sites. *Wind Energy*. 2021;24(11):1315-1336.
53. Verma AS, Jiang Z, Caboni M, Verhoef H, van der Mijle Meijer H, Castro SGP, Teuwen JJE. A probabilistic rainfall model to estimate the leading-edge lifetime of wind turbine blade coating system. *Renew Energy*. 2021;178:1435-1455.
54. Im H, Kim B. Numerical study on the effect of blade surface deterioration by erosion on the performance of a large wind turbine. *J Renew Sustain Energy*. 2019;11(6):063308.
55. Campobasso MS, Castorrini A, Cappugi L, Bonfiglioli A. Experimentally validated three-dimensional computational aerodynamics of wind turbine blade sections featuring leading edge erosion cavities. *Wind Energy*. 2022;25(1):168-189.
56. Orrell A, Preziuso D, Foster N, Morris S, Homer J. 2018 Distributed Wind Market Report, U.S. Department of Energy, office of Energy Efficiency & Renewable Energy; 2018.
57. Mishnaevsky LJ. Repair of wind turbine blades: review of methods and related computational mechanics problems. *Renew Energy*. 2019;140:828-839.
58. Stephenson S. Wind blade repair: planning, safety, flexibility. Composites World; 2011.
59. Qblade code main page. http://www.q-blade.org/
60. Chaudhary MK, Roy A. Design & optimization of a small wind turbine blade for operation at low wind speed. *World J Eng*. 2015;12(1):83-94.
61. Khaled M, Ibrahim MM, Elsayed H, Hamed A. Aerodynamic design and blade angle analysis of a small horizontal–axis wind turbine. *Am J Modern Energy*. 2017;3(July):23-37.
62. Torrano I. Low speed wind tunnel design, setup, validation and testing of airfoils in turbulent in ow conditions. *Ph.D. Thesis*: Mondragon Goi Eskola Politeknikoa; 2016.
63. Zarketa-Astigarraga A, Martin-Mayor A, Martinez-Agirre M. Experimental uncertainty decompositions of aerodynamic coefficients affected by operative condition variations. *Measurement*. 2020;165(C):1-14.
64. Zhang X, Li Z, Yu X, Li W. Aerodynamic performance of trailing-edge modification of H-type VAWT blade considering camber effect. *Int J Aeronaut Space Sci*. 2020;21(3):587-598.
65. Sun J, Huang D. Numerical investigation of boundary layer suction control positions on airfoils for vertical-axis wind turbine. *J Mech Sci Technol*. 2021; 35(7):2903-2914.
66. Vaidyanathan A, Kingman D, Kurth T. When do endplates work? In: 52nd Aerospace Sciences Meeting; 2014:1-11.
67. Boermans LMM. Research on sailplane aerodynamics at Delft University of Technology. Recent and present developments. *Techn Soar*. 2006;30(1-2): 1-25.
68. Zarketa-Astigarraga A, Martin-Mayor A, Martinez-Agirre M, Peñalba-Retes M. Assessing the statistical validity of momentum-deficit-based c_D measurements in turbulent configurations. *Measurement*. 2021;181:109592.
69. González MA, Ezquerro JM, Lapuerta V, Laverón A, Rodríguez J. Components of a wind tunnel balance: design and calibration. *Wind Tunnels Exper Fluid Dyn Res*. 2011;2011:1-20.
70. Meseguer-Ruiz J, Sanz-Andrés A. Procedimientos para determinar numéricamente la resistencia. *Aerodinámica básica*. 2nd ed.: Garceta Grupo Editorial; 2012:262-264.
71. Labview software main page. https://www.ni.com/en-us/shop/labview.html
72. Zarketa-Astigarraga A, Martin-Mayor A, Martinez-Agirre M. Theoretical concepts for describing a replication-levels-based uncertainty analysis approach. In: Yurish S, ed. *Advances in measurements and instrumentation: Reviews, book series*. 1st ed., Vol. 2: IFSA Publishing; 2020.
73. Glauert H. Airplane propellers. *Aerodynamic theory: A general review of progress under a grant of the Guggenheim Fund for the promotion of aeronautics*. Berlin, Heidelberg: Springer Berlin Heidelberg; 1935.
74. Manwell JF, McGowan JG, Rogers AL. *Wind Energy Explained Theory, Design and Application*. 2nd ed.: Wiley & Sons; 2011.
75. Viterna LA, Corrigan RD. Fixed Pitch Rotor Performance of Large Horizontal Axis Wind Turbines, Cleveland, Ohio, USA, NASA; 1982.

76. Waloddi Weibull B. A statistical distribution function of wide applicability. *J Appl Mech*. 1951;18:293-297.
77. Tuller SE, Brett AC. The characteristics of wind velocity that favor the fitting of a Weibull distribution in wind speed analysis. *J Climate Appl Meteorol*. 1983;23:124-134.
78. Habali SM, Saleh IA. Local design, testing and manufacturing of small mixed airfoil wind turbine blades of glass fiber reinforced plastics: part I: design of the blade and root. *Energy Convers Manag*. 2000;41:249-280.

How to cite this article: Zarketa-Astigarraga A, Penalba M, Martin-Mayor A, Martinez-Agirre M. Impact of turbulence and blade surface degradation on the annual energy production of small-scale wind turbines. *Wind Energy*. 2023;26(12):1217-1234. doi:10.1002/we.2866